Thermodynamic stability and contributions to the Gibbs free energy of nanocrystalline Ni_3Fe

Stefan H. Lohaus,[1,*] Michel B. Johnson,[2] Peter F. Ahnn,[1] Claire N. Saunders,[1] Hillary L. Smith,[3] Mary Anne White,[2,4] and Brent Fultz[1,†]

[1]*Department of Applied Physics and Materials Science, California Institute of Technology, Pasadena, California 91125, USA*
[2]*Clean Technologies Research Institute, Dalhousie University, Halifax, Nova Scotia, Canada B3H 4R2*
[3]*Department of Physics and Astronomy, Swarthmore College, Swarthmore, Pennsylvania 19081, USA*
[4]*Department of Chemistry, Dalhousie University, Halifax, Nova Scotia, Canada B3H 4R2*

(Received 11 September 2019; revised 10 January 2020; accepted 21 July 2020; published 11 August 2020)

The heat capacities of nanocrystalline Ni_3Fe and control materials with larger crystallites were measured from 0.4–300 K. The heat capacities were integrated to obtain the enthalpy, entropy, and Gibbs free energy and to quantify how these thermodynamic functions are altered by nanocrystallinity. From the phonon density of states (DOS) measured by inelastic neutron scattering, we find that the Gibbs free energy is dominated by phonons and that the larger heat capacity of the nanomaterial below 100 K is attributable to its enhanced phonon DOS at low energies. Besides electronic and magnetic contributions, the nanocrystalline material has an additional contribution at higher temperatures, consistent with phonon anharmonicity. The nanocrystalline material shows a stronger increase with temperature of both the enthalpy and entropy compared to the bulk sample. Its entropy exceeds that of the bulk material by 0.4 k_B/atom at 300 K. This is insufficient to overcome the enthalpy of grain boundaries and defects in the nanocrystalline material, making it thermodynamically unstable with respect to the bulk control material.

DOI: 10.1103/PhysRevMaterials.4.086002

I. INTRODUCTION

The structure and properties of nanomaterials usually differ significantly from their bulk counterparts, and these differences can be exploited in devices with novel functionalities. For example, as engineered devices become smaller, they become composite nanomaterials with new structures and properties. The nanoscale is often a bridge between atomistic behavior and continuum properties. Thermodynamic questions include how atomic vibrations become heat and how this affects the Gibbs free energy of a nanomaterial, which determines its thermodynamic stability. How stable or unstable are nanostructures at modest temperatures? To date the Gibbs free energy of nanostructured materials is poorly understood, even though it underlies their stability and their suitability for service in engineered devices.

Most of the entropy of nanostructured materials is vibrational in origin, although there is some configurational entropy from structural degrees of freedom [1]. Vibrational spectra of nanoparticles have been studied for some time, and the large literature on this subject [2–42] is surveyed in Sec. II C below. The vibrational entropy is changed by dynamical degrees of freedom in nanocrystalline structures and should be of thermodynamic importance to the Gibbs free energy. The usual trend is for the vibrational spectra of a nanomaterial to have more low-energy vibrations than its bulk counterpart, giving larger vibrational amplitudes of atoms in the nanomaterial and a larger vibrational entropy at a given temperature. This lowers the Gibbs free energy of nanomaterials at finite temperature, but quantifying the thermodynamic consequences remains a challenge.

Because smaller particles have larger surface-to-volume ratios and higher internal energy per atom, adding an atom to a small particle is less favorable than adding it to a large one. The "Gibbs-Thomson effect" raises the chemical potential of atoms in small particles (and for nearby atoms in local equilibrium with them). Grain growth occurs when these differences in chemical potential cause a diffusive flux from small particles to large particles. Extra contributions to the enthalpy from elastic fields and internal defects are also expected in many as-synthesized nanomaterials. The excess enthalpy of nanomaterials can be measured by heating in a calorimeter to high temperatures, transforming the nanomaterial into a material with larger crystallites [4–8].

The Fe-Ni phase diagram (see Supplemental Material [43]) is important for steel metallurgy, and the Invar alloy of Fe-36%Ni was the topic for the 1920 Nobel Prize in Physics. The Ni-rich alloys are fcc solid solutions at most temperatures. Below 773 K, Ni_3Fe can become chemically long-range-ordered with the $L1_2$ structure (where Fe atoms occupy the corners, and the Ni atoms the faces, of the standard fcc cube) [44]. The $L1_2$ order develops sluggishly by a first-order phase transition [45,46], requiring for example heat treatments with over two months of annealing time [44]. An fcc solid solution is commonplace at ambient conditions, and fcc solid solutions of Ni_3Fe have several advantages for studying the thermodynamics of nanocrystals. Some of the smallest nanocrystal sizes in metals, 6–7 nm, can be obtained in Ni_3Fe prepared by high energy ball milling [47]. This method can prepare the rela-

*slohaus@caltech.edu
†btf@caltech.edu

tively large quantities of nanocrystalline powders required for neutron scattering experiments, and these alloys collect less oxygen and hydrogen that impair inelastic neutron scattering measurements. Ball milling produces Ni_3Fe with a disordered fcc structure [48]. Disordered Ni_3Fe is ferromagnetic up to 871 K [46]. Nanomaterials have lower Curie temperatures and the ferromagnetic transition of nanocrystalline Ni_3Fe has been observed between 728 K [49] and 848 K [50].

Here we report new thermodynamic results from cryogenic calorimetry measurements on a nanocrystalline material and its bulk counterpart with larger crystallites. The results are analyzed to obtain the enthalpy, entropy, and Gibbs free energies, and their difference for the two materials. By combining inelastic neutron scattering measurements with calorimetry results, we quantify the change in vibrational entropy with nanocrystallinity. Neutron scattering experiments measured the phonon density of states of control and nanocrystalline materials, showing that the difference in entropy of nanocrystalline and bulk Ni_3Fe is dominated by vibrational entropy. We also assess the electronic and magnetic contributions to the free energy of Ni_3Fe and how these are changed by nanocrystallinity.

We show an excess entropy of the nanocrystalline Ni_3Fe that lowers its Gibbs free energy, but this entropic stabilization is opposed by the excess enthalpy from grain boundaries and defects. Altogether, the nanocrystalline material has a larger Gibbs free energy than the bulk control material at 300 K, making the nanocrystalline material thermodynamically unstable at ambient conditions.

II. THERMODYNAMICS OF NANOPARTICLES

A. Heat capacity and free energy

Equilibrium in a material at a temperature T and ambient pressure p is found at the minimum of its Gibbs free energy:

$$G(T) = H_p(T) - TS_p(T)\,. \tag{1}$$

The enthalpy H_p and the entropy S_p have opposite effects on the value of G and therefore opposite effects on the stability. Both can be determined from the heat capacity C_p with the relationships:

$$H_p(T) = H_0 + \int_0^T C_p(T')dT', \tag{2}$$

$$S_p(T) = S_0 + \int_0^T \frac{C_p(T')}{T'}dT'. \tag{3}$$

The thermodynamic stability of a nanomaterial with respect to a bulk control material is determined by the difference $\Delta G^{\mathrm{n-c}}$ (a positive $\Delta G^{\mathrm{n-c}}$ makes the nanomaterial unstable with respect to the control material):

$$\begin{aligned}\Delta G^{\mathrm{n-c}}(T) &= G^{\mathrm{n}}(T) - G^{\mathrm{c}}(T)\\ &= \Delta H_p^{\mathrm{n-c}}(T) - T\Delta S_p^{\mathrm{n-c}}(T),\end{aligned} \tag{4}$$

$$\Delta H_p^{\mathrm{n-c}}(T) = \Delta H_0^{\mathrm{n-c}} + \int_0^T \Delta C_p^{\mathrm{n-c}}(T')dT'\,, \tag{5}$$

$$\Delta S_p^{\mathrm{n-c}}(T) = \Delta S_0^{\mathrm{n-c}} + \int_0^T \frac{\Delta C_p^{\mathrm{n-c}}(T')}{T'}dT', \tag{6}$$

where a notation such as $\Delta C_p^{\mathrm{n-c}}$ denotes the difference in heat capacity of the nanocrystalline material and the control bulk material at constant pressure. The larger H_0 of the nanocrystalline material originates from grain boundaries, internal stresses, and defects.

The metastable nanomaterial cannot access all its degenerate configurational microstates at low temperatures, since it is kinetically trapped in its own metabasin. At 0 K the material is in one microstate, corresponding to a specific nanocrystalline configuration [51–53]. According to Boltzmann's definition of entropy, $S = k_{\mathrm{B}} \ln \Omega$, where k_{B} is the Boltzmann constant and Ω is the number of accessible microstates, the resulting residual entropy at 0 K is zero because $\Omega = 1$. Therefore $\Delta S_0^{\mathrm{n-c}} = 0$, in agreement with the Third Law. An alternative viewpoint of a finite residual configurational entropy at 0 K is presented in Sec. IV A.

B. Internal energy and entropy of nanocrystals

Grain boundaries force atoms into irregular local coordinations, increasing their internal energies. Metals with stronger bonding and higher melting temperatures are generally expected to have grain boundaries with higher energies. From work on a number of grain boundary structures in fcc metals, the grain boundary energy varies from approximately 0.4 to 1.2 $\mathrm{J/m^2}$ in the sequence Au, Ag, Al, Pd, Cu, Co, Ni, Pt [54,55]. For fcc Ni metal, however, grain boundaries between crystals with various orientations have energies that span much of this entire range [56].

High energy ball milling produces nonequilibrium nanomaterials by severe plastic deformation. This process creates microstructural features that contribute to the internal energy and consequently increase the enthalpy of nanomaterials. Point defects such as vacancies are likely, although they have not been reported. Impurities such as interstitial atoms are introduced during ball milling, and line defects such as dislocations are responsible for some of the low-angle boundaries between crystallites, although their density within the crystals may be low [4–7]. Twin boundaries are also possible [6,8]. Microstructural features give a distribution of internal energies to the different crystallites of both bcc and fcc phases of Ni-Fe alloys [9]. These microstructural sources of internal energy contribute to H_0 of Eq. (2).

Entropy counteracts the enthalpy to lower the Gibbs free energy, and has configurational, magnetic, electronic, and vibrational contributions. During the cryogenic calorimetric measurements, atom mobilities are suppressed, and there are no changes in the atomic configurations. We therefore do not measure differences in the configurational entropy between the nanostructured material and the control samples. The magnetic Curie temperature is at 871 K, so only a small amount of magnetic entropy is expected around 300 K, as discussed below. The heat goes primarily into atom vibrations.

C. Prior work on vibrations in nanomaterials

From prior work, we know that the phonon DOS, $g(\varepsilon)$, of a nanocrystalline material differs from that of bulk materials in three ways. These three features have been found for isolated nanoparticles and for consolidated nanoparticles with

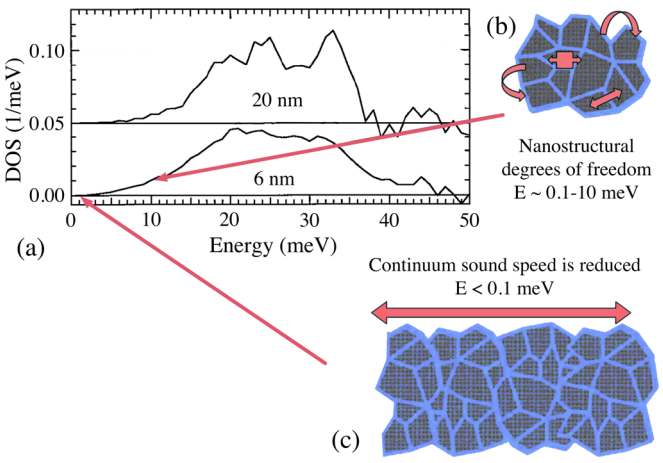

FIG. 1. (a) Phonon DOS from a polycrystalline powder of an fcc Ni-Fe alloy [3]. Compared to the DOS from the material with the larger 20 nm crystallite size, the 6 nm DOS shows three features: (1) enhancement of the intensity below 15 meV, (2) broadening of all features, (3) a tail of spectral weight above 36 meV. (b) Representative librational or vibrational modes of the nanocrystalline microstructure, with energies of order 1 meV and wavelengths of 10 nm. (c) Continuum behavior at long wavelengths.

grain boundaries between them. They are found in metals, semiconductors, and insulators, and all three are seen in Fig. 1(a). They are:

(1) An enhancement of $g(\varepsilon)$ at low energies [e.g., below 15 meV in Fig. 1(a)].

(2) A general broadening of sharp features in $g(\varepsilon)$ (e.g., at 24 and 33 meV).

(3) A tail in $g(\varepsilon)$ that extends to high energies above the usual cutoff frequency of longitudinal phonon modes (e.g., 36 meV).

Feature 1 is understood best. An enhancement of $g(\varepsilon)$ at low energies is expected from the degrees of freedom in a nanostructure, as depicted in Fig. 1(b). Modes of the nanostructure may originate with the vibrations of nanocrystals against each other, mutual rotations, or with the partial confinement of vibrational waves to boundary regions, similar to Rayleigh waves at surfaces with elastic discontinuities. This enhancement disappears at very low energies when the wavelengths are longer than the nanostructural features [Fig. 1(c)], so the material behaves as a continuum with altered elastic constants [57–63].

Both calculations and measurements on either isolated nanocrystals or nanocrystals with rigid constraints showed an enhancement of modes at low energies [13–42]. This low-energy regime sometimes indicates a change in the dimensionality of the vibrational modes. Fitting the low-energy part of $g(\varepsilon)$ to ε^n has given $n < 2$, i.e., smaller than for three-dimensional vibrations [23,25,39]. This exponent n can be close to 1.0 as expected for two-dimensional vibrations [22,32,64]. This is not a universal result, however, and often $n \simeq 2$ in consolidated nanocrystals [3,29]. Nevertheless, more modes are found at low energies, sometimes by a factor of five or so [3,18,20,21,24,29,32,35,36,38,39]. As discussed below, transferring phonon spectral weight from higher energies to lower energies causes an increase in the vibrational entropy as calculated by Eq. (7), because the Planck factor $n_{\varepsilon,T}$ is largest at low ε.

Feature 2, the broadening of features in the $g(\varepsilon)$ of nanomaterials, is less understood. This broadening has been attributed to the shortening of phonon lifetimes, which could explain both features 2 and 3 [21]. In a crystal smaller than 10 nm, a phonon propagates only tens of atomic distances before it encounters a surface or grain boundary. If the phonon is scattered at the interface by effects of disorder or anharmonicity, its lifetime may be only tens of vibrational periods or less. The spectral shape of a damped harmonic oscillator function has an asymmetrical broadening about the central frequency that can often account for the broadened phonon DOS of nanostructured materials [2,3,21,31–35,40,41,65].

Feature 3 may be attributable to the same phonon lifetime broadening, but other explanations have been proposed. Some prior work indicated that these tails in $g(\varepsilon)$ originate from harmonic modes at high frequencies caused by surface oxides or impurities [26,32,36,38,42]. High energy tails of the phonon DOS have also been reported in a number of molecular dynamics simulations on pure materials [19,23,27,30,38] and have been attributed to higher frequency harmonic vibrations of atoms at surfaces of nanoparticles.

III. EXPERIMENTAL METHODS AND RESULTS

A. Materials

Inelastic neutron scattering measurements of phonon densities of states typically require several grams of material. High energy ball milling has proved practical for preparing relatively large amounts of material with small crystals. These crystals are consolidated into larger particles of powder. The relatively low surface areas of the powders make them less prone to adsorption of gases and water, which would impede neutron scattering measurements.

To prepare the nanocrystalline Ni_3Fe samples, powders of Ni (75 atomic%) and Fe (25 atomic%) were mixed with 5 wt.% stearic acid or ethanol and sealed in a steel vial. Ball milling was performed with a Fritsch Planetary Mono Mill for 20 h at 650 rpm using steel ball-to-powder weight ratios between 20:1 and 40:1. After milling, the material was sonicated in isopropyl alcohol and centrifuged to remove the stearic acid. We call the nanomaterials prepared by high energy ball milling "as-milled" samples. Control samples of bulk material with larger crystallites can be prepared by milling the powder for shorter times, by milling with a lower ball-to-powder ratio, or by annealing the as-milled material in sealed quartz ampoules under vacuum.

In previous work, nanocrystalline Ni_3Fe samples prepared by a similar method were well characterized by inelastic neutron scattering, small-angle neutron scattering, transmission electron microscopy, x-ray diffractometry, Mössbauer spectrometry, and magnetization [2–4].

Transmission electron microscopy (TEM) images of the nanocrystalline sample, shown in Figs. 2(a) and 2(b) are direct evidence of their nanocrystallinity. The TEM analysis from previous work [Fig. 2(c)] determined a mean crystallite size of 6 nm [3].

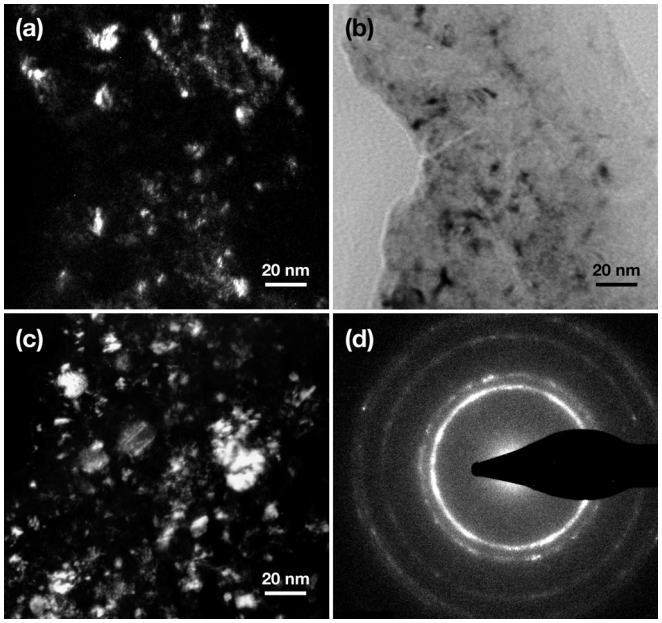

FIG. 2. Transmission electron microscopy images of the as-milled Ni_3Fe. The dark-field (DF) and bright-field (BF) images were obtained with the (111) fcc diffraction. (a) DF and (b) BF images of the as-milled sample, compared to (c) DF image from previous work, with crystallites of 6 nm [3]. (d) Electron diffraction pattern.

X-ray diffraction (XRD) measurements using Cu K_α radiation were performed on all materials. Figure 3 shows the XRD patterns obtained from a sample in the as-milled state and from the same sample after annealing at 873 K for 1 h. The diffraction data show main peaks from an fcc solid solution. There is evidence for some $L1_2$ chemical order in a few of the annealed control samples, seen as superlattice peaks in the XRD pattern. This, however, should not alter the phonon DOS significantly [44,66,67]. Other control samples did not show this $L1_2$ chemical order and all control samples gave very similar curves of $C_p(T)$ as shown below in Fig. 4.

To determine the grain sizes of our materials, the broadening of the diffraction peaks caused by the small crystallites

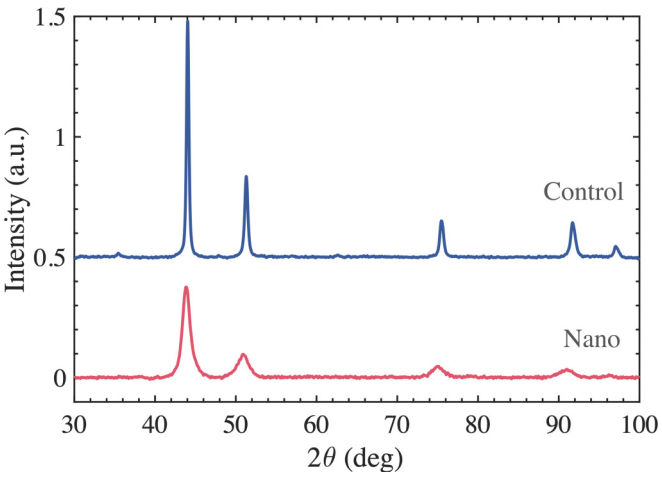

FIG. 3. X-ray diffraction patterns of the as-milled material and of the bulk control sample after annealing at 873 K for 1 h.

was separated from strain broadening using the Williamson-Hall method [68]. We modified the Williamson-Hall method to include anisotropic strains [69], based on anisotropic elastic constants of Ni_3Fe reported in [70]. The grain sizes were determined by comparing the grain size broadening of our samples with those from previous work with crystallites of 6 nm using the Scherrer equation [69]. Our nanomaterials and bulk control samples have grain sizes of 6–7 nm and 25–35 nm, respectively. The detailed calculations can be found in the Supplemental Material [43], together with the dependence of the grain sizes and strains on the annealing temperature.

The lattice parameters depend inversely on the grain sizes of the samples. They were computed from the the XRD patterns using the Nelson-Riley method [69]. The as-milled samples have lattice parameters between 3.587–3.604 Å, in good agreement with values reported for ball-milled Ni_3Fe (3.600 Å [71] and 3.590 Å [48]). The annealed control samples have a lattice parameter of 3.5599 Å, slightly larger than the lattice parameter of 3.5533 Å reported for a Ni_3Fe single crystal [70]. The grain size dependence of the lattice parameter is also presented with the Supplemental Material [43].

B. Heat capacity

Specific heat measurements were made by relaxation microcalorimetry using a commercial instrument, a physical property measurement system (PPMS, from Quantum Design, San Diego). Measurements were conducted in the temperature range between 0.4 and 300 K over which accuracy, with due care, can be within 1% from 5 K to 300 K, and 5% from 0.4 K to 5 K [72]. Measurements were taken in two modes: ^{4}He cooling for the 2–300 K temperature interval and ^{3}He cooling for the interval from 0.5–10 K. To enhance the thermal contact between the sample and the microcalorimeter, a thin layer of Apiezon N grease was applied to the sample stage and its contribution to the specific heat is accounted for during addendum measurements prior to each sample measurement. All measurements were conducted under high vacuum (10^{-5} Torr) to minimize convective heat losses.

For the relaxation calorimetry measurements, the as-milled powder samples were consolidated into pellets using a 0.28 cm diameter die. An appropriate amount of powder was added to the die and hydraulically pressed with a force of 2700 N, resulting in a pressure of approximately 0.45 GPa. The consolidated samples had better thermal contact and heat transfer and allowed for more accurate mass determinations owing to ease of handling without sample loss during transfers. The mass of each pellet was measured (Sartorius semimicro balance), and the pellet was transferred onto the sample stage and lightly pressed into the grease film. The sample masses ranged from 10 to 27 mg.

Several heat capacity measurements were performed on nanocrystalline (as-milled) and control samples (less milled or annealed). The results are shown in Fig. 4. There are some variations between samples of each type, but in all cases the heat capacity curves for the nanocrystalline material exceeded the heat capacity of the control samples. This difference was most evident at low temperatures, as expected owing to the enhanced phonon DOS at low energies.

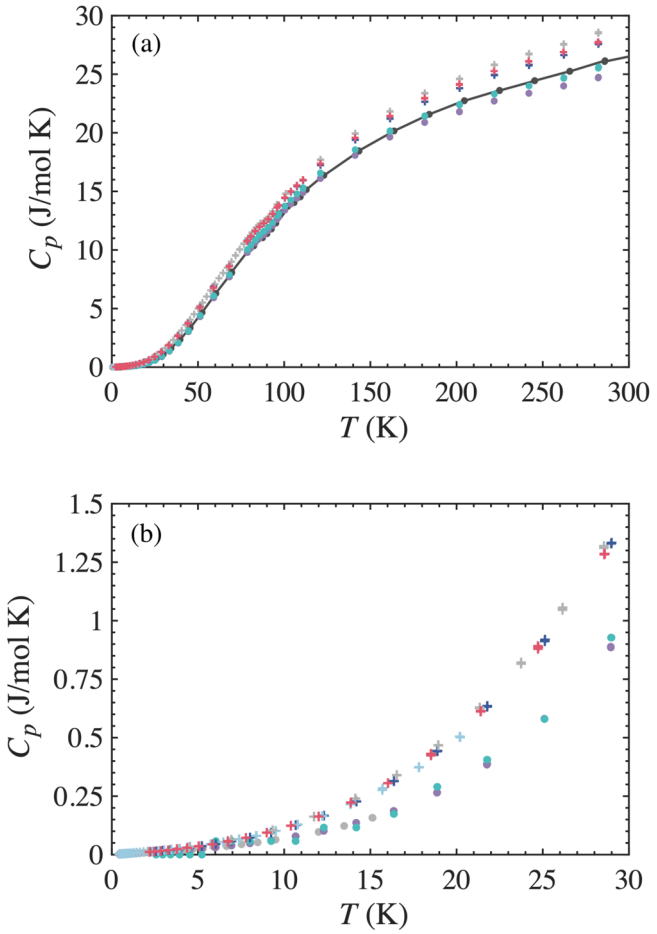

FIG. 4. Heat capacity of Ni_3Fe measured by calorimetry for the as-milled materials (+) and large-grained control samples (•), normalized by the number of moles of atoms. Different colors represent results from different samples. (a) Full data sets. The solid black curve is from the annealed control material (see text). (b) Low-temperature data.

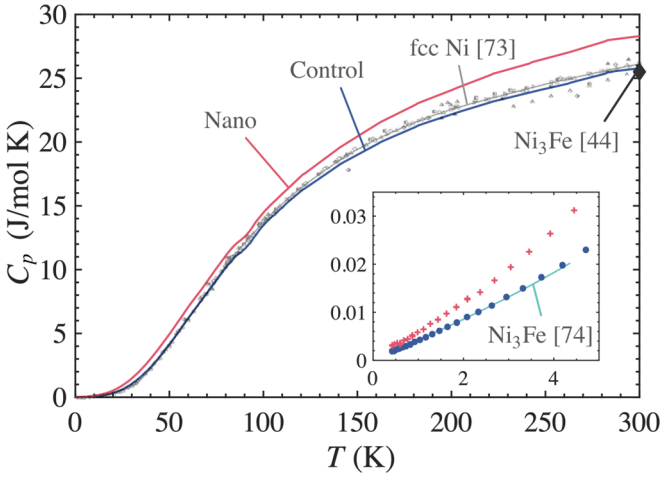

FIG. 5. Mean heat capacities of the as-milled nanomaterial and control bulk sample compared to literature. The heat capacity of bulk disordered Ni_3Fe reported by Kollie and Brooks [44] is shown at 300 K (♦). Data compiled by Desai for fcc Ni are shown as small markers and the recommended curve as a thin solid line [73]. The inset compares our low temperature data (<5 K) with the fit reported by Kollie *et al.* [74].

The heat capacity of the as-milled nanocrystalline material was also enhanced at temperatures above 200 K. We were concerned that this could be from interstitial impurities, carbon and oxygen, that were introduced into the material by milling. This motivated the preparation of control samples by annealing the as-milled material at 873 K to increase the crystallite size and eliminate defects, resulting in a bulk control sample with the same interstitial atoms as the nanomaterial. The concentration of impurities in both the as-milled and annealed samples were indeed the same as measured by an instrumental gas analysis performed by a commercial laboratory (the results are included in the Supplemental Material [43]). The heat capacity of this annealed control sample, shown in Fig. 4 as a solid line, is similar to that of the other samples of Ni_3Fe with large crystals, however, indicating that the enhanced heat capacity above 200 K does not originate from interstitial impurities.

Figure 5 compares our heat capacities with those found in the literature. Our measured heat capacity for the control sample is similar to the heat capacity measured on fcc Ni [73] and in good agreement with the heat capacity of 25.5 J/(mol K) measured for Ni_3Fe at 300 K [44]. Low temperature measurements on disordered Ni_3Fe [74] are in excellent agreement with the heat capacity of our control sample.

A complete $L1_2$ ordering transition in this material would reduce the heat capacity by approximately 0.1 k_B/atom (0.8 J/mol K) at 300 K [44], with most of this from phonons [67]. However, the $L1_2$ ordering in Ni_3Fe is very sluggish. It is a first-order transition, so with partial order, the change in heat capacity would be reduced proportionately. We therefore neglect the effects of partial chemical ordering on the heat capacity of our samples.

C. Defect recovery and grain growth

Differential scanning calorimetry (DSC) was performed using a Perkin Elmer DSC 7 to quantify the internal enthalpy difference ΔH_0^{n-c} of Eq. (5), associated with defects and grain boundaries. The as-milled nanomaterial with grain sizes of 7 nm was placed in the DSC sample holder inside alumina crucibles using a N_2 purge gas flowing at 20–30 ml/min. The differential heat flow to the sample was measured while heating it from 320 K to 800 K at 20 K/min. The heat evolution of the nanomaterial measured by DSC is shown in Fig. 6.

The defect recovery and grain growth are exothermic and irreversible processes, so subsequent DSC runs on the same sample lack the exothermic peak between 580–750 K, indicating that the entire defect recovery occurred during the first run. To quantify the enthalpy resulting from defects and grain growth, a linear baseline was used to calculate the area of the highlighted exothermic peak. The resulting enthalpy is $H_0^{n-c} = 2.3$ kJ/mol. This is in very good agreement with the re-crystallization enthalpy of 2.2 kJ/mol of ball-milled Ni_3Fe reported in [75].

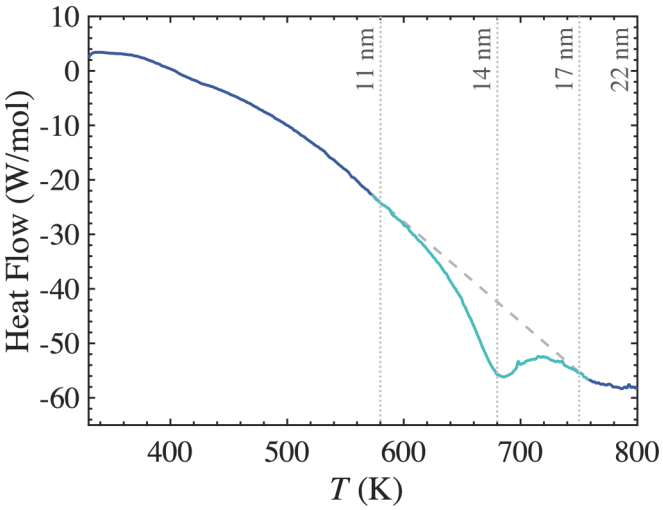

FIG. 6. Heat flow measured by DSC while heating the nanocrystalline sample at 20 K/min. Positive values correspond to endothermic heat flows. The release of internal energy from defects and grain growth is highlighted (green) and its enthalpy of $H_0^{n-c} = 2.3$ kJ/mol was calculated using a linear baseline (dashed line). The labeled grain sizes were determined from measured XRD patterns presented in the Supplemental Material [43].

The Curie transition of nanocrystalline $Ni_{0.7}Fe_{0.3}$ was reported to occur at 728 K [49]. Even though we did not measure the thermal evolution of the magnetism in our samples, some endothermic signal around 720 K could correspond to the ferromagnetic transition. The Curie temperature of nanocrystalline materials, however, is sensitive to the exact grain size [76], and it might be different in our materials. If the highlighted signal of Fig. 6 includes the magnetic transition, the calculation of H_0^{n-c} would be affected. To estimate this possible error, we calculated the enthalpy of the magnetic transition using the heat capacity measurement of Ni_3Fe by Kollie *et al.* [44]. The resulting magnetic enthalpy is 0.12 kJ/mol, which corresponds to 5% of H_0^{n-c}.

We showed that the highlighted exothermic peak of Fig. 6 corresponds indeed to grain growth of the nanocrystalline material by heating the as-milled material to different temperatures and acquiring XRD patterns after cooling. The nanomaterial was heated in vacuum at 20 K/min, the same heating rate used for the DSC measurement. The XRD patterns showed sharpening of the diffraction peaks with increasing annealing temperatures. The grain size broadening of the XRD peaks were separated from the strain broadening using a Williamson-Hall method modified for anisotropic strain fields (these calculations and the measured XRD patterns are included in the Supplemental Material [43]). The resulting grain sizes, included in Fig. 6, reveal that most of the grain growth during heating occurs indeed between 580 and 800 K.

D. Phonon density of states

Inelastic neutron scattering (INS) measurements were performed on powder samples with the time-of-flight wide angular-range chopper spectrometer, ARCS, at the Spallation Neutron Source at Oak Ridge National Laboratory. An incident energy of 70 meV was used. The powder sample was placed in an aluminum can with a cylindrical insert to create an annulus of sample 1 mm in thickness, with 30 mm of outer diameter and 50 mm of height. Measurements were performed in a low-background closed cycle refrigerator (CCR 16) between 190 K and 300 K. Data reduction was performed with DGS reduction in Mantid [77]. The data were normalized by the proton current on target. Bad detector pixels were identified and masked, and the data were corrected for detector efficiency using a measurement from vanadium. The phonon density of states (DOS) curves were obtained after subtraction of the empty aluminum can and corrections for multiphonon and multiple scattering using the *Multiphonon* package [78].

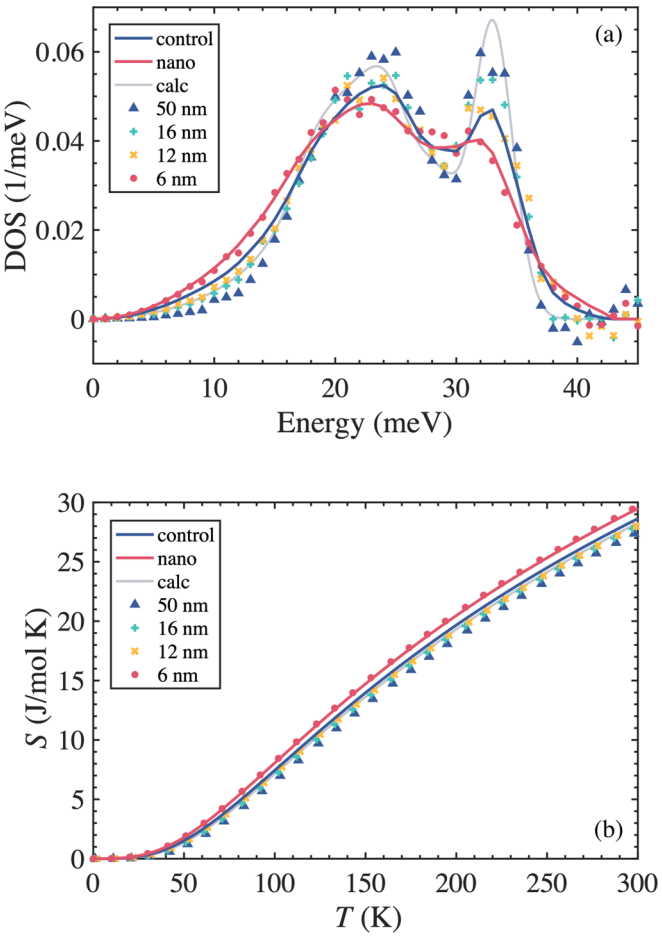

FIG. 7. (a) Phonon DOS curves measured by inelastic neutron scattering at 300 K. Solid curves correspond to the new measurements performed at ARCS, while the markers are measurements from previous work [3]. The solid light curve (Calc), also from previous work, was calculated with a Born-von Kármán model using force constants from [66] and broadened by instrument resolution. (b) Phonon entropies calculated with the curves of panel a, using Eq. (7).

The measured phonon DOS are presented in Fig. 7(a) as solid curves together with DOS from prior work as markers and a gray solid curve calculated with a Born-von Kármán model [3]. The phonon spectra from prior work were obtained by INS measured only at two values of momentum transfer.

This resulted in an underestimation of the DOS at low energies especially for the large grained materials, due to the sharper features in their spectra. Both spectra obtained for the nanocrystalline material ('nano' and '6 nm') are in good agreement.

The vibrational contribution to the entropy $S_{\rm vib}$ and heat capacity $C_{p,\rm vib}$ can be determined from the phonon DOS, $g(\varepsilon)$, as [1,10–12]

$$S_{\rm vib}(T) = 3k_{\rm B}\int_0^\infty g(\varepsilon)[(1+n_{\varepsilon,T})\ln(1+n_{\varepsilon,T}) - n_{\varepsilon,T}\ln n_{\varepsilon,T}]\,d\varepsilon, \tag{7}$$

$$C_{p,\rm vib}(T) = 3N\,k_{\rm B}\int_0^\infty g(\varepsilon)\left(\frac{\varepsilon}{k_{\rm B}T}\right)^2\frac{e^{\varepsilon/k_{\rm B}T}}{(e^{\varepsilon/k_{\rm B}T}-1)^2}\,d\varepsilon, \tag{8}$$

where ε is the phonon energy and $n_{\varepsilon,T} = (\exp(\varepsilon/k_{\rm B}T)-1)^{-1}$ the Planck distribution of phonon occupancy. The phonon DOS, $g(\varepsilon)$, is normalized to 1, and N is the number of atoms in the sample.

Figure 7(b) shows the resulting vibrational entropies, which as expected, are enhanced with increasing nanocrystallinity. The entropy obtained for the control sample is larger than that from previous work ('50 nm'). The previous underestimation of the DOS at low energies causes a reduction of the vibrational entropy as calculated by Eq. (7), because the Planck factor $n_{\varepsilon,T}$ is largest at low ε.

IV. DISCUSSION

A. Residual entropy at 0 K

The nanocrystalline material is at a metastable equilibrium. Its configurational degrees of freedom are not equilibrated and are unchanged between 0 K and approximately 580 K, when the heat evolution from defect annihilation and grain growth is observed. This heat evolution shown in Fig. 6 can be integrated to give 0.4 $k_{\rm B}$/atom, which could be used as a residual entropy at 0 K. However, the configuration of the nanocrystalline material is frozen below 580 K, so this residual entropy does not contribute to the free energy because it has no ability to do work. Furthermore, all of the heat capacity below 300 K is accounted for by phonons, electrons, and magnetism (as discussed in the next sections), and an additional 0.4 $k_{\rm B}$/atom is well outside the experimental errors.

A residual entropy calculated by integrating the heat capacity as $\Delta S = \int C_p/T\,dT$ assumes an equilibrated system, which is not the case for the configurational degrees of freedom. Even though many possible configurations are thermodynamically allowed, corresponding to a high degree of degeneracy, the nanomaterial is kinetically trapped. It can access only its own metastable basin, which at 0 K consists of a single microstate [51–53]. Boltzmann's entropy definition, $S = k_{\rm B}\ln\Omega$, which is consistent with the second law of thermodynamics for nonequilibrated systems [79] gives $S_0^n = 0$ for the configurational degrees of freedom of our nanocrystalline material when $\Omega = 1$ at 0 K.

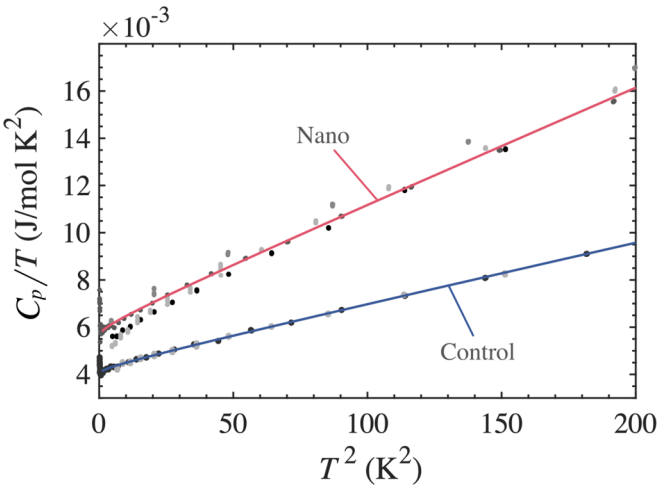

FIG. 8. Low temperature heat capacities of the nanocrystalline and control materials plotted as C_p/T vs T^2. Solid curves are fits to the data using Eq. (9).

B. Contributions to the heat capacity at low temperatures

Phonons, electrons, and magnetism all contribute to the heat capacity in the low temperature region between 0.4–10 K as

$$C_p(T) = C_{p,\rm el} + C_{p,\rm mag} + C_{p,\rm ph} = \gamma T + \alpha T^{3/2} + \beta T^3. \tag{9}$$

Fits of Eq. (9) to the data are shown in Fig. 8 for the nanocrystalline and control materials, plotted as C_p/T vs T^2. Figure 8 shows a vertical offset from conduction electrons, with a linear behavior from phonons ($\gamma T + \beta T^3$). The contribution from magnons becomes pronounced only at very low temperatures around 1 K [74]. Nevertheless, including the spin wave term $\alpha T^{3/2}$ in fits with Eq. (9) reduces the overall RMS errors of the fits by 20% for the bulk material and 15% for the nanocrystalline material. Both fits, with and without the magnon term, their fitting parameters and RMS errors can be found in the Supplemental Material [43].

Our control sample has an electronic contribution of $\gamma = 3.96$ mJ/(mol K^2), in good agreement with the $\gamma = 4.05$ mJ/(mol K^2) reported in [74] and $\gamma = 3.90$ mJ/(mol K^2) [80]. The electronic heat capacity of the nanocrystalline material is larger, with $\gamma = 5.55$ mJ/(mol K^2).

The phonon contribution gives $\beta = 2.51\times10^{-2}$ mJ/(mol K^4) for the control sample, corresponding to a Debye temperature of $\theta_D = 426$ K. Kollie *et al.* [74] reported Debye temperatures between 430 K and 488 K, and Gupta [81] reported $\theta_D = 425$ K. The enhanced degrees of freedom of the nanomaterial at low vibrational energies are manifested in a larger Debye fitting parameter of $\beta = 4.81\times10^{-2}$ mJ/(mol K^4), corresponding to a $\theta_D = 327$ K. These Debye temperatures can be used to estimate a vibrational entropy difference at high temperatures as

$$\Delta S^{\rm n-c} = 3\,k_{\rm B}\ln\left(\frac{\theta_D^{\rm c}}{\theta_D^{\rm n}}\right) = 0.8\,k_{\rm B}/\text{atom}\ , \tag{10}$$

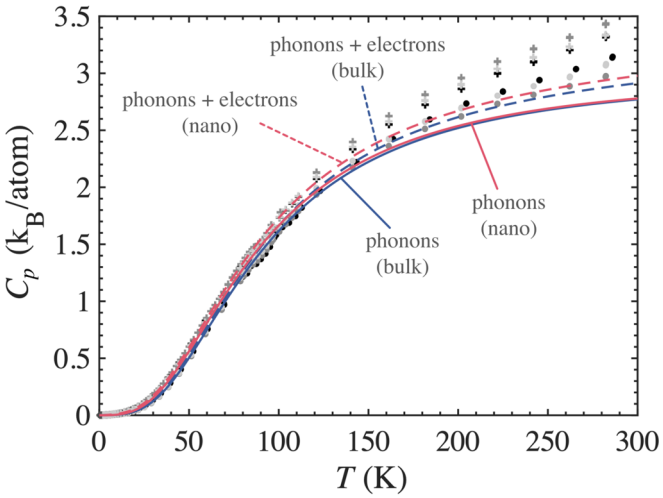

FIG. 9. Heat capacities of nanomaterial (+) and control samples (•) from calorimetry shown in Fig. 5, superposed with phonon heat capacities calculated from the phonon DOS using Eq. (8) (solid lines) and with vibrational plus electronic heat capacities (dashed lines).

but this is unrealistically large compared to what we obtain by considering the full phonon spectra of the two materials.

The spin wave contribution found by fitting our data gave $\alpha = 0.16$ mJ/(mol K$^{5/2}$) for the control, and $\alpha = 0.27$ mJ/(mol K$^{5/2}$) for the nanocrystalline material. The value for the control material is a little larger than reported by Kollie [74] [$\alpha = 0.10$ mJ/(mol K$^{5/2}$)] and Dixon [80] [$\alpha = 0.12$ mJ/(mol K$^{5/2}$)]. The lowest temperatures achieved in their experiments were 1.2 K and 1.4 K, respectively. Since the magnon contribution is most evident at very low temperatures, their fits might have underestimated the magnon contribution.

C. Contributions to the heat capacity at higher temperatures

The phonon contribution to the heat capacity was calculated from the phonon DOS measured by inelastic neutron scattering using Eq. (8). The resulting vibrational heat capacities for the nanocrystalline and control samples are compared in Fig. 9 to the total heat capacities measured by calorimetry. For the control material approximately 90% of the heat capacity originates from phonons (80% for the nanomaterial). The increase of heat capacity above the classical limit of 3 k_B/atom at high temperatures requires more than harmonic or quasiharmonic phonons calculated by Eq. (8), as discussed in the next section.

In what follows, we show that adding the contributions from electrons and spins to the phonon contribution brings the heat capacity of our materials into much better agreement with results from calorimetry. The electronic contribution to the heat capacity is estimated by extrapolating the low temperature electronic contribution ($C_{p,\mathrm{el}} = \gamma T$) to higher temperatures. The results for both the nanocrystalline and control materials are included in Fig. 9. At 300 K, the electronic heat capacities for the nanocrystalline and control samples are 0.20 k_B/atom and 0.14 k_B/atom, respectively.

Estimating the magnetic contribution at 300 K is not so easy, since the contribution from spin waves, $C_{p,\mathrm{mag}} = \alpha T^{3/2}$, is not applicable at elevated temperatures. The heat released by disordering the spins below the Curie transition is reflected in the temperature dependence of the magnetization. Most of the change in magnetization occurs near the Curie temperature, so the magnetic thermal disorder is small at 300 K. The ferromagnetic transition of disordered bulk Ni_3Fe occurs at 871 K [46]. Experimental measurements show a decrease of only 5% in the spontaneous magnetization of bulk Ni_3Fe between 0 K and 300 K [82].

The structural disorder in nanocrystalline materials is responsible for some decrease in lattice magnetization and Curie temperatures with respect to bulk materials. Curie temperatures between 728 K [49] and 848 K [50] have been reported for nanocrystalline Ni_3Fe. Previous measurements on our nanocrystalline samples at 300 K showed that the magnetization is 7% lower than that of the control samples [4]. In other work, at 4 K the magnetization of a nanocrystalline sample (12.5 nm) was found to be 2% lower than that of a sample with larger grain sizes [50].

The total entropy of magnetic disordering was computed by integrating the magnetic heat capacity of bulk Ni_3Fe reported in [83] up to 1400 K, giving $S_{\mathrm{mag,tot}} = 0.61\ k_B$/atom. We estimate the fraction of this magnetic entropy in our materials below 300 K with the mean field approximation, using the mean field entropy $S_{\mathrm{mf}} = k_B \ln \Omega$, where Ω is the number of equivalent spin configurations. For a fully magnetized material at 0 K ($M = 1$), all the spins are aligned, so $\Omega = 1$ and $S_{\mathrm{mf}} = 0$. Above the Curie transition $M = 0$, with half of the spins in each direction. The entropy is then $S_{\mathrm{mf}} = Nk_B \ln 2$, where N is the total number of atoms. For partial magnetization:

$$M = \frac{(+1)\,xN + (-1)\,N(1-x)}{N} = 2x - 1, \qquad (11)$$

where x denotes the fraction of atoms with spin up. The mean field entropy can be written as a function of $M(T)$:

$$\begin{aligned} S_{\mathrm{mf}}(M) &= -Nk_B[x \ln x + (1-x)\ln(1-x)] \\ &= -\frac{Nk_B}{2}\left[(M+1)\ln\frac{M+1}{2} + (1-M)\ln\frac{1-M}{2}\right] \end{aligned} \qquad (12)$$

The fraction of the total magnetic entropy is the ratio $S_{\mathrm{mf}}(M)/S_{\mathrm{mf}}(0)$, so the magnetic entropy of our materials can be computed as:

$$S_{\mathrm{mag}}(M) = \frac{S_{\mathrm{mf}}(M)}{Nk_B \ln 2} S_{\mathrm{mag,tot}}. \qquad (13)$$

For bulk Ni_3Fe, we used experimental data for $M(T)$ [82] with Eq. (13) to obtain the entropy from 0–300 K. At 300 K it is $S^{\mathrm{c}}_{\mathrm{mag}} = 0.09\ k_B$/atom. Magnetization data were available for the nanomaterial at 4 K [50] and 300 K [4]. The small decrease in magnetization from 4 to 300 K of the nanomaterial was used with Eq. (13) to obtain the entropy at 300 K of $S^{\mathrm{n}}_{\mathrm{mag}} = 0.15\ k_B$/atom.

The magnetic heat capacity of our control sample was computed between 0–300 K from $S^{\mathrm{c}}_{\mathrm{mag}}(T)$. It is presented with the other contributions in Fig. 10(a). Our magnetic contribution at 300 K (0.12 k_B/atom) is in good agreement with the magnetic heat capacity of Ni_3Fe reported by Kollie (0.14 k_B/atom)

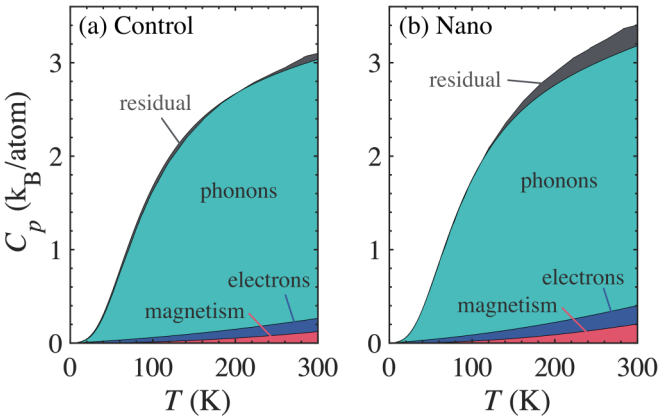

FIG. 10. Individual contributions to the heat capacity of (a) the control and (b) nanocrystalline samples. The residual is the difference between the sum of the labeled contributions and the total heat capacity measured by calorimetry.

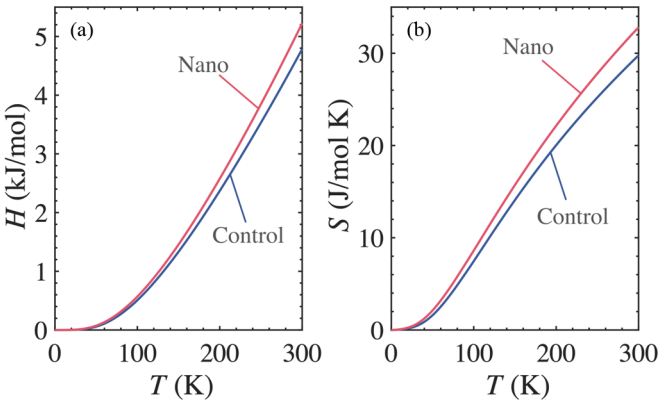

FIG. 11. (a) Total enthalpy and (b) entropy of nanocrystalline material and control sample computed from calorimetry measurements of the heat capacity using Eqs. (2) and (3). The grain boundary enthalpy H_0 is not included.

[83] and the magnetic contribution calculated by Körmann *et al.* for Ni (0.11 k_B/atom) [84]. As seen from the small residual of Fig. 10(a), the sum of magnetic, electronic, and phononic contributions agrees well with the total heat capacity measured by calorimetry.

For the nanocrystalline material, the magnetic entropy was calculated only at 4 K and 300 K. By assuming that it follows the same temperature dependence as the control material, we estimated its magnetic heat capacity between 0–300 K. The individual contributions to the heat capacity of the nanomaterial can be seen in Fig. 10(b). As suggested by the larger residual heat capacity at 300 K, the nanocrystalline material has additional contributions, besides the electronic, magnetic, and vibrational heat capacities. This residual heat capacity is 0.22 k_B/atom at 300 K, corresponding to a residual entropy of 0.14 k_B/atom. Its origin is discussed in the next section.

D. Contributions from thermal expansion and anharmonicity

It is straightforward to calculate the contribution to the heat capacity from thermal expansion [1]:

$$\Delta C_p^{\mathrm{te}}(T) = C_p(T) - C_v(T) = Bv\beta^2 T. \qquad (14)$$

Using a bulk modulus of 179 GPa, molar volume of 6.75 cm^3/mol, volume thermal expansion of 3.3×10^{-5}/K (values for Ni_3Fe at 300 K taken from [70]), gives $\Delta C_p^{\mathrm{te}} =$ 0.05 k_B/atom, about 1% of the total heat capacity at 300 K and about 20% of the residual heat capacity of the nanomaterial. Thermal expansion alone cannot account for the excess residual heat capacity of Fig. 10(b).

Another possible contribution comes from anharmonic phonons. Phonons may have reduced lifetimes from anharmonic interactions with grain boundaries or other defects of the nanomaterial, broadening the features of the DOS as shown in Fig. 7(a). The phonon heat capacities and entropies calculated with Eqs. (7) and (8) assume a distribution of harmonic modes and do not account for shortened phonon lifetimes. Lifetime broadening can be modeled using damped harmonic oscillators, and the introduction of damping causes a shift of the spectrum to higher energies, giving an apparent reduction in the entropy when calculated with Eq. (7). A correction for this effect, given in Ref. [85], predicts an increase of the phonon entropy by 0.15 k_B/atom for a damped harmonic oscillator with a damping factor of $\mathcal{Q} =$ 6, which is generally consistent with the broadened phonon DOS of the nanocrystalline material. Shortened phonon lifetimes account well for the residual entropy of 0.14 k_B/atom for the nanomaterial at 300 K. An anharmonic contribution of a fraction of one k_B/atom is typical for metals at high temperatures [86].

E. Gibbs free energy and stability

The H_0 term in Eq. (2) is an important contribution to the enthalpy of the nanocrystalline material. It was measured to be 2.3 kJ/mol by the heat evolved when the nanocrystalline material was heated to 800 K, as the grains grew and the defects were annihilated (Fig. 6). The enthalpy $H_p(T)$ was obtained by integrating the heat capacity as in Eq. (2), and it is shown in Fig. 11(a). The difference of $H_p(T)$ between the nanocrystalline and control material, $\Delta H_p^{\mathrm{n-c}}(T)$, increases with temperature.

The entropy of formation of a grain boundary is positive, helping to stabilize a consolidated nanomaterial at finite temperatures by Eq. (1). The excess entropy of the nanomaterial obtained from calorimetry can be seen in Fig. 11(b). At 300 K it is 0.37 k_B/atom (3.0 J/mol K). An early report gave a larger excess entropy for nanocrystalline Pd [57]. Isolated iron nanoparticles showed an increase of phonon entropy of 0.5 k_B/atom [8]. Our measured excess entropy contributes to the Gibbs free energy with $-T\Delta S^{\mathrm{n-c}} = -0.9$ kJ/mol at 300 K. The excess entropy increases with temperature, so its contribution to the Gibbs free energy should be larger at 600 K where the grain growth starts.

Figure 12 shows that the excess Gibbs free energy $\Delta G^{\mathrm{n-c}}(T)$ (labeled "Diff") is positive at all temperatures. The nanocrystalline material has a larger entropy, and a larger enthalpy, than the control sample. The net effect is to reduce the $\Delta G^{\mathrm{n-c}}(T)$ with temperature somewhat but not enough to overcome the enthalpy H_0 from grain boundaries and defects in the nanocrystalline material. By extrapolating the measured Gibbs free energies to 600 K, we predict that

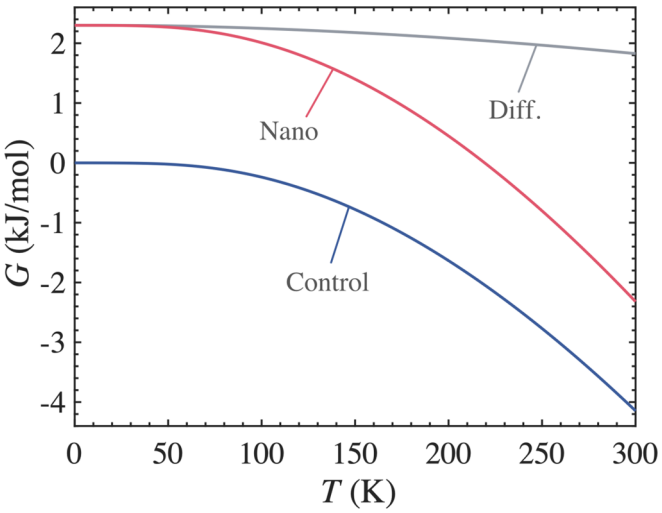

FIG. 12. Gibbs free energies of as-milled nanocrystalline Ni_3Fe and control sample, using enthalpies and entropies of Fig. 11, and $\Delta H_0^{n-c} = 2.3$ kJ/mol.

the nanomaterial would still be thermodynamically unstable. Its larger excess entropy at 600 K would be insufficient to overcome the enthalpy of its grain boundaries (2.3 kJ/mol). Since diffusion is thermally activated, the grains start to grow at 600 K, transforming the metastable nanomaterial into its stable counterpart with larger crystallites.

V. CONCLUSIONS

The heat capacities of nanocrystalline and large-grained fcc Ni_3Fe alloys were measured between 0.4–300 K. The heat capacity of the nanocrystalline material was consistently larger, especially at temperatures below 100 K. This difference originates from its larger phonon density of states (DOS) at energies below 15 meV, as shown by old and new inelastic neutron scattering measurements. Phonons accounted for most of the heat capacities of the Ni_3Fe samples and for most of the difference between the nanocrystalline and control samples. The remaining heat capacity of the control sample was accounted for by electronic and magnetic contributions. Adding all components of the nanocrystalline material (phonons, electrons, and magnetism) gave a result that was about 7% lower than the total measured by calorimetry at 300 K. This difference is attributed to a larger phonon anharmonicity in the nanocrystalline material, which could also cause the observed broadening of features in its measured phonon spectrum. The larger entropy of the nanocrystalline material with respect to the control sample is counteracted by its larger enthalpy, so the difference in Gibbs free energy between the nanocrystalline and control sample decreases only modestly with temperature. The nanocrystalline material is thermodynamically unstable at temperatures to 300 K and is probably unstable to higher temperatures where grain growth occurs.

ACKNOWLEDGMENTS

This work was supported by the Department of Energy through the Office of Science, Basic Energy Sciences Grant DE-FG02-03ER46055. M.A.W. acknowledges support from the Natural Sciences and Engineering Research Council of Canada (Grant No. RGPIN-2015-04593), the Canada Foundation for Innovation, and the Clean Technologies Research Institute at Dalhousie University.

[1] B. Fultz, *Phase Transitions in Materials* (Cambridge University Press, Cambridge, 2014).
[2] H. N. Frase, L. J. Nagel, J. L. Robertson, and B. Fultz, Philos. Mag. B **75**, 335 (1995).
[3] H. N. Frase, B. Fultz, and J. L. Robertson, Phys. Rev. B **57**, 898 (1998).
[4] H. N. Frase, Ph.D. thesis, California Institute of Technology, 1998. Download at https://thesis.library.caltech.edu/301/.
[5] H. J. Fecht, Nanostruct. Mater. **6**, 33 (1995).
[6] O. Boytsov, A. I. Ustinov, E. Gaffet, and F. Bernard, J. Alloys Compounds **432**, 103 (1998).
[7] J. Y. Huang, Y. K Wu, and H. Q. Ye, Microscopy Res. Technique **40**, 101 (1998).
[8] B. Roldan Cuenya, L. K. Ono, J. R. Croy, K. Paredis, A. Kara, H. Heinrich, J. Zhao, E. E. Alp, A. T. DelaRiva, A. Datye, E. A. Stach, W. Keune *et al.*, Phys. Rev. B **86**, 165406 (2012).
[9] L. B. Hong and B. Fultz, J. Appl. Phys. **79**, 3946 (1996).
[10] D. C. Wallace, *Thermodynamics of Crystals* (Dover, Mineola, New York, 1998).
[11] A. van de Walle and G. Ceder, Rev. Mod. Phys. **74**, 11 (2002).
[12] B. Fultz, Prog. Mater. Sci. **55**, 247 (2010).
[13] W. D. Kristensen, E. J. Jensen, and R. M. J. Cotterill, J. Chem. Phys. **60**, 4161 (1974).
[14] A. Tamura, K. Higeta, and T. Ichinokawa, J. Phys. C **15**, 4975 (1982).
[15] A. Tamura, K. Higeta, and T. Ichinokawa, J. Phys. C **16**, 1585 (1983).
[16] K. Suzuki and K. Sumiyama, Mater. Trans. JIM **36**, 188 (1995).
[17] B. Fultz, L. Anthony, L. J. Nagel, R.M. Nicklow, and S. Spooner, Phys. Rev. B **52**, 3315 (1995).
[18] J. Trampenau, K. Bauszus, W. Petry, and U. Herr, J. Nanostruct. Mater. **6**, 551 (1995).
[19] D. Wolf, J. Wang, S. R. Phillpot, and H. Gleiter, Phys. Rev. Lett. **74**, 4686 (1995).
[20] B. Fultz, J. L. Robertson, T. A. Stephens, L. J. Nagel, and S. Spooner, J. Appl. Phys. **79**, 8318 (1996).
[21] B. Fultz, C. C. Ahn, E. E. Alp, W. Sturhahn, and T. S. Toellner, Phys. Rev. Lett. **79**, 937 (1997).
[22] U. Stuhr, H. Wipf, K. H. Andersen, and H. Hahn, Phys. Rev. Lett. **81**, 1449 (1998).
[23] A. Kara and T. S. Rahman, Phys. Rev. Lett. **81**, 1453 (1998).
[24] E. Bonetti, L. Pasquini, E. Sampaolesi, A. Deriu, and G. Cicognani, J. Appl. Phys. **88**, 4571 (2000).

[25] P. M. Derlet, R. Meyer, L. J. Lewis, U. Stuhr, and H. Van Swygenhoven, Phys. Rev. Lett. **87**, 205501 (2001).

[26] L. Pasquini, A. Barla, A. I. Chumakov, O. Leupold, R. Ruffer, A. Deriu, and E. Bonetti, Phys. Rev. B **66**, 073410 (2002).

[27] R. Meyer, S. Prakash, and P. Entel, Phase Transitions **75**, 51 (2002).

[28] R. Meyer, L. J. Lewis, S. Prakash, and P. Entel, Phys. Rev. B **68**, 104303 (2003).

[29] A. B. Papandrew, A. F. Yue, B. Fultz, I. Halevy, W. Sturhahn, T. S. Toellner, E. E. Alp, and H. K. Mao, Phys. Rev. B **69**, 144301 (2004).

[30] A. Kara, A. N. Al-Rawi, and T. S. Rahman, J. Comp. Theor. Nanoscience **1**, 216 (2004).

[31] P. Machnikowski and L. Jacak, Phys. Rev. B **71**, 115309 (2005).

[32] B. Roldan Cuenya, A. Naitabdi, J. Croy, W. Sturhahn, J.Y. Zhao, E. E. Alp, R. Meyer, D. Sudfeld, E. Schuster, and W. Keune, Phys. Rev. B **76**, 195422 (2007).

[33] S. Stankov, Y. Z. Yue, M. Miglierini, B. Sepiol, I. Sergueev, A. I. Chumakov, L. Hu, P. Svec, and R. Ruffer, Phys. Rev. Lett. **100**, 235503 (2008).

[34] B. Roldan Cuenya, W. Keune, R. Peters, E. Schuster, B. Sahoo, U. von Hoersten, W. Sturhahn, J. Zhao, T. S. Toellner, E. E. Alp, and S. D. Bader, Phys. Rev. B **77**, 165410 (2008).

[35] B. Roldan Cuenya, J. R. Croy, L. K. Ono, A. Naitabdi, H. Heinrich, W. Keune, J. Zhao, W. Sturhahn, E. E. Alp, and M. Hu, Phys. Rev. B **80**, 125412 (2009).

[36] B. Roldan Cuenya, L. K. Ono, J. R. Croy, A. Naitabdi, H. Heinrich, J. Zhao, E. E. Alp, W. Sturhahn, and W. Keune, Appl. Phys. Lett. **95**, 143103 (2009).

[37] S. Stankov, M. Sladecek, T. Slezak, J. Lazewski. R. Röhlsberger, B. Sepiol, G. Vogl, A. I. Chumakov, R. Rüffer, and N. Spiridis, J. Phys. Conf. Series **217**, 012144 (2010).

[38] S. Stankov, M. Miglierini, A. I. Chumakov, I. Sergueev, Y. Z. Yue, B. Sepiol, P. Svec, L. Hu, and R. Ruffer, Phys. Rev. B **82**, 144301 (2010).

[39] H. L. Smith, B. C. Hornbuckle, L. Mauger, B. Fu, S. J. Tracy, G. B. Thompson, M. S. Lucas, Y. Xiao, M. Y. Hu, J. Zhao, E. E. Alp, and B. Fultz, Acta Mater. **61**, 7466 (2013).

[40] Qi-C. Sun, D. Mazumdar, L. Yadgarov, R. Rosentsveig, R. Tenne, and J. L. Musfeldt, Nano Lett. **13**, 2803 (2013).

[41] S. De, K. Kunal, and N. R. Aluru, J. Appl. Phys. **119**, 114304 (2016).

[42] R. Carles, P. Benzo, B. Pecassou, and C. Bonafos, Sci. Rep. **6**, 39164 (2017).

[43] See Supplemental Material at http://link.aps.org/supplemental/10.1103/PhysRevMaterials.4.086002 for details on our samples, the analysis of the XRD measurements, a discussion on the heat capacity results, as well as the full heat capacity data set.

[44] T. G. Kollie and C. R. Brooks, Phys. Stat. Solidi A **19**, 545 (1973).

[45] A. G. Khachaturyan, Progress in Material Science **22**, 1 (1978).

[46] R. J. Wakelin and E. L. Yates, Proc. Phys. Soc. B **66**, 221 (1953).

[47] H. Ouyang, Ph.D. thesis, California Institute of Technology, 1993. Download at https://thesis.library.caltech.edu/3304/.

[48] C. N. Chinnasamy, A. Narayanasamy, N. Ponpandian, K. Chattopadhyay, and M. Saravanakumar, Materials Science Engineering A **304-306**, 408 (2001).

[49] P. Y. Li, H. M. Lu, Z. H. Cao, S. C. Tang, X. K. Meng, X. S. Li, and Z. H. Jiang, Appl. Phys. Lett. **94**, 213112 (2009).

[50] I. Chicinas, V. Pop, and O. Isnard, J. Magn. Magn. Mater. **242-245**, 885 (2002).

[51] D. Kivelson and H. Reiss, J. Phys. Chem. B **103**, 8337 (1999).

[52] J. C. Mauro, R. J. Loucks, and S. Sen, J. Chem. Phys **133**, 164503 (2010).

[53] P. K. Gupta and J. C. Mauro, J. Chem. Phys **129**, 067101 (2008).

[54] H. Van Swygenhoven, D. Farkas, and A. Caro, Phys. Rev. B **62**, 831 (2000).

[55] M. Yuasa, T. Nakazawa, and M. Mabuchi, J. Phys.: Condens. Matter **24**, 265703 (2012).

[56] D. Olmsted, S. M. Foiles, and E. A. Holm, Acta Mater. **57**, 3694 (2009).

[57] D. Korn, A. Morsch, R. Birringer, W. Arnold, and H. Gleiter, J. Phys. Colloques **49**, C5-769 (1988).

[58] T. D. Shen, C. C. Koch, T. Y. Tsui, and G. M. Pharr, J. Mater. Res. **10**, 2892 (1995).

[59] G. E. Fougere, L. Riester, M. Ferber, J. R. Weertman, and R. W. Siegel, Mater. Sci. Eng. A **204**, 1 (1995).

[60] P. G. Sanders, J. A. Eastman, and J. R. Weertman, Acta Mater. **45**, 4019 (1997).

[61] H. S. Cao, J. J. Hunsinger, and O. Elkedim, Scr. Mater. **46**, 55 (2002).

[62] H. Tanimoto, S. Sakai, E. Kita, and H. Mizubayashi, Mater. Trans. **44**, 94 (2003).

[63] A. F. Yue, A. Papandrew, O. Delaire, B. Fultz, Z. Chowdhuri, R. M. Dimeo, and D. A. Neumann, Phys. Rev. Lett. **93**, 205501 (2004).

[64] N. Spiridis, M. Zajac, P. Piekarz, A. I. Chumakov, K. Freindl, J. Goniakowski, A. Koziol-Rachwal, K. Parlinski, M. Slezak, T. Slezak, U. D. Wdowik, D. Wilgocka-Slezak, and J. Korecki, Phys. Rev. Lett. **115**, 186102 (2015).

[65] R. Rohlsberger, W. Sturhahn, T. S. Toellner, K. W. Quast, P. Hession, M. Hu, J. Sutter, and E. E. Alp, J. Appl. Phys. **86**, 584 (1999).

[66] E. D. Hallman and B. N. Brockhouse, Can. J. Phys. **47**, 1117 (1969).

[67] M. S. Lucas, L. Mauger, J. A. Muńoz, I. Halevy, J. Horwath, S.L. Semiatin, S. O. Leontsev, M. B. Stone, D. L. Abernathy, Yuming Xiao, Paul Chow, and B. Fultz, J. Appl. Phys. **113**, 17A308 (2013).

[68] H. P. Klug and L. E. Alexander, *X-Ray Diffraction Procedures* (Wiley-Interscience, New York, 1974).

[69] B. Fultz and J. Howe, *Transmission Electron Microscopy and Diffractometry of Materials* (Springer, Heidelberg, 2013).

[70] P. Turchi, Y. Calvayrac, and F. Plicque, Phys. Status Solidi A **45**, 229 (1978).

[71] C. N. Chinnasamy, A. Narayanasamy, K. Chattopadhyay, and N. Ponpandian, Nanostruct. Mater. **12**, 951 (1999).

[72] C. A. Kennedy, M. Stanescu, R. A. Marriott, and M. A. White, Cryogenics **47**, 107 (2007).

[73] P. D. Desai, Int. J. Thermophys. **8**, 763 (1987).

[74] T. G. Kollie, J. O. Scarborough, and D. L. McElroy, Phys. Rev. B **2**, 2831 (1970).

[75] F. Popa, O. Isnard, I. Chicinas, and V. Pop, J. Alloys Compd. **554**, 39 (2013).

[76] H. M. Lu, P. Y. Li, Y. N. Huang, X. K. Meng, X. Y. Zhang, and Q. Liu, J. Appl. Phys. **105**, 023516 (2009).

[77] O. Arnold, J. C. Bilheux, J. M. Borreguero, A. Buts, S. I. Campbell, L. Chapon, M. Doucet, N. Draper, R. Ferraz Leal, M. A. Gigg, V. E. Lynch, A. Markvardsen, D. J. Mikkelson, R. L. Mikkelson, R. Miller, K. Palmen, P. Parker, G. Passos, T. G. Perring, P. F. Peterson, S. Ren, M. A. Reuter, A. T. Savici, J. W. Taylor, R. J. Taylor, R. Tolchenov, W. Zhou, and J. Zikovsky, Nucl. Instrum. Methods Phys. Res., A **764**, 156 (2014).

[78] Multiphonon package available at: https://github.com/sns-chops/multiphonon.

[79] S. Goldstein and J. L. Lebowitz, Physica D **193**, 53 (2004).

[80] M. Dixon, F. E. Hoare, and T. M. Holden, Proc. R. Soc. London A **303**, 339 (1968).

[81] K. P. Gupta, C. H. Cheng, and P. A. Beck, Journal of Physics Chemistry of Solids **25**, 73 (1964).

[82] J. J. Went, Physica **17**, 596 (1951).

[83] T. G. Kollie, Doctoral Dissertation, University of Tennessee - Knoxville, 1969.

[84] F. Körmann, A. Dick, T. Hickel, and J. Neugebauer, Phys. Rev. B **83**, 165114 (2011).

[85] M. Palumbo, B. Burton, A. Costa e Silva, B. Fultz, B. Grabowski, G. Grimvall, B. Hallstedt, and O. Hellmann, Phys. Stat. Solidi B **251**, 14 (2014).

[86] D. C. Wallace, *Statistical Physics of Crystals and Liquids* (World Scientific, Singapore, 2002), Chap. 19.